arXiv:1407.1743v1 [astro-ph.SR] 7 Jul 2014

Phase mixing of Alfvén waves near a 2D magnetic null point

J. A. McLaughlin

Department of Mathematics & Information Sciences, Northumbria University, Newcastle Upon Tyne, NE1 8ST, UK

Abstract:
The propagation of linear Alfvén wave pulses in an inhomogeneous plasma near a 2D coronal null point is investigated. When a uniform plasma density is considered, it is seen that an initially planar Alfvén wavefront remains planar, despite the varying equilibrium Alfvén speed, and that all the wave collects at the separatrices. Thus, in the non-ideal case, these Alfvénic disturbances preferentially dissipate their energy at these locations. For a non-uniform equilibrium density, it is found that the Alfvén wavefront is significantly distorted away from the initially planar geometry, inviting the possibility of dissipation due to phase mixing. Despite this however, we conclude that for the Alfvén wave, current density accumulation and preferential heating still primarily occur at the separatrices, even when an extremely non-uniform density profile is considered.

Keywords: Magnetohydrodynamics (MHD) – Waves – Magnetic fields – Sun: atmosphere – Corona

1 Introduction

MHD wave propagation within an inhomogeneous medium is a fundamental plasma process and the study of MHD waves in the neighbourhood of magnetic null points directly contributes to this area (see McLaughlin *et al.* 2011a for a comprehensive review of the topic). *Null points* are weaknesses in the magnetic field at which the field strength, and thus the Alfvén speed, is zero. *Separatrices* are topological features that separate regions of different magnetic connectivity, and are an inevitable consequence of the isolated magnetic flux fragments in the photosphere. The number of resultant null points depends upon the complexity of the magnetic flux distribution, but tens of thousands are estimated to be present (see, e.g., Close *et al.* 2004; Longcope 2005; Régnier *et al.* 2008; Longcope & Parnell 2009).

In addition, MHD wave perturbations are ubiquitary in the solar corona (e.g. Tomczyk *et al.* 2007) and a variety of observations have clearly demonstrated the existence of wave activity for all three of the basic waves modes; namely Alfvén waves and fast and slow magnetoacoustic waves. That the waves exist is no longer in doubt but the surprising fact is that these are generally rapidly damped. Waves in a uniform magnetic field and plasma have extremely long damping lengths and so the explanation for the observations must lie in the non-uniform nature of the solar corona. Non-thermal line broadening and narrowing due to Alfvén waves has been reported by various authors, including Banerjee *et al.* (1998), Erdélyi *et al.* (1998), Harrison *et al.* (2002) and O'Shea *et al.* (2003; 2005). The role of Alfvén waves in coronal heating through dissipation and observed spectral line broadening has been reported both analytically (e.g. Dwivedi & Srivastava 2006) and more recently numerically (e.g. Chmielewski *et al.* 2013, and references therein).

Thus, MHD waves and magnetic topology *will* encounter each other in the corona (e.g. waves emanating from a flare or CME will at some point encounter a coronal null point). The behaviour

of linear MHD waves (fast & slow magnetoacoustic waves and Alfvén waves) has been investigated in the neighbourhood of a variety of 2D null points (e.g. McLaughlin & Hood 2004; 2005; 2006a; 2006b; McLaughlin *et al.* 2008). These authors found that the (linear) Alfvén wave propagates along magnetic fieldlines and accumulates along the separatrices in 2D, or along the spine or fan-plane in 3D. Thus, these authors make a key prediction: *separatrices, spines and/or fan-planes will be locations for preferential heating by (linear) Alfvén waves*.

Waves in the neighbourhood of a single 2D null point have also been investigated using cylindrical models, in which the generated waves encircled the null point (e.g. Bulanov & Syrovatskii 1980; Craig & McClymont 1991; 1993; Craig & Watson 1992; Hassam 1992) and it was found that the wave propagation leads to an exponentially-large increase in the current density (see also Ofman *et al.* 1993; Steinolfson *et al.* 1995 and a comprehensive review by McLaughlin *et al.* 2011a for further details). Nonlinear and three-dimensional MHD wave activity about coronal null points has also been investigated (e.g. Galsgaard *et al.* 2003; Pontin & Galsgaard 2007; Pontin *et al.* 2007; McLaughlin *et al.* 2008; 2009; Galsgaard & Pontin 2011a; 2011b; Thurgood & McLaughlin 2012; 2013).

One of the most efficient damping mechanisms of Alfvén waves to date is called *phase mixing* and is described by Heyvaerts & Priest (1983) for a harmonic wave train propagating in a uniform vertical magnetic field. They found that the amplitudes decay as the negative exponential depending on the third power of the height and linearly with magnetic resistivity, η. Thus, the damping length depends on $\eta^{-1/3}$. Since observations rarely show more than a few periods at a time, Hood *et al.* (2002) investigated the propagation of single pulses and found that the decay was now algebraic in nature but still dependent on $\eta^{-1/3}$.

The phase mixing mechanism is simple to explain; when the plasma has a density gradient perpendicular to the magnetic field, the Alfvén speed is a function of the transverse coordinate. Thus, the Alfvén waves propagate on each fieldline with their own local Alfvén speed. After a certain time, the Alfvén wave perturbations on neighbouring fieldlines become out of phase (e.g. Botha *et al.* 2000; McLaughlin *et al.* 2011b). It is precisely the Alfvén perturbations oscillating independently from their neighbours that leads to the build-up of small length scales and consequently current generation and hence dissipation.

In this paper, we will investigate the behaviour of the linear Alfvén wave in the neighbourhood of a simple 2D X-point geometry, and we shall consider the behaviour in both uniform and non-uniform density plasma. This lifts one of the key restrictions imposed by McLaughlin & Hood (2004) and its subsequent papers, namely the assumption of constant equilibrium density. With a non-uniform density profile, the Alfvén speed is now changing from fieldline to fieldline, and thus we may have phase mixing. This is the key question that this paper addresses: with the addition of a non-uniform density, does the current build-up still occur at the separatrix or does phase mixing now allow the energy to be extracted from a different location?

Our paper has the following outline: the basic setup, equations and assumptions are described in §2, the numerical and analytical results are presented in §3, and the conclusions are given in §4.

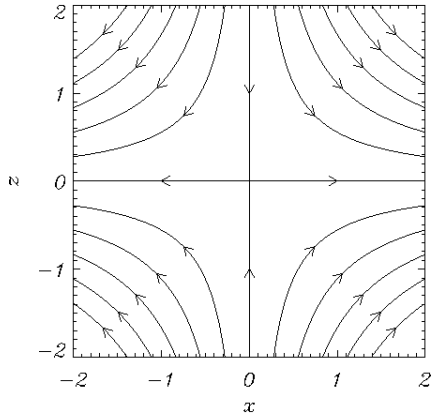

Figure 1: Equilibrium magnetic field.

2 Basic Equations

The MHD equations for a low-β plasma appropriate to the solar corona are used. Hence,

$$\begin{aligned} \rho\left[\frac{\partial \mathbf{v}}{\partial t}+(\mathbf{v}\cdot\nabla)\mathbf{v}\right] &= \frac{1}{\mu}(\nabla\times\mathbf{B})\times\mathbf{B}, \\ \frac{\partial \mathbf{B}}{\partial t} &= \nabla\times(\mathbf{v}\times\mathbf{B})+\eta\nabla^2\mathbf{B}, \\ \frac{\partial \rho}{\partial t}+\nabla\cdot(\rho\mathbf{v}) &= 0, \qquad \nabla\cdot\mathbf{B}=0, \end{aligned} \tag{1}$$

where ρ is the mass density, $\mathbf{v}$ is the plasma velocity, $\mathbf{B}$ the magnetic induction (usually called the magnetic field), $\mu = 4\pi\times 10^{-7}\mathrm{Hm}^{-1}$ the magnetic permeability, $\eta = 1/\mu\sigma$ is the magnetic diffusivity $(\mathrm{m}^2\mathrm{s}^{-1})$, and σ the electrical conductivity. The gas pressure and the adiabatic energy equation are neglected in the low-β approximation. We have also neglected viscous terms in equations (1). Investigations involving viscous magnetofluids can be found in Kumar & Bhattacharyya (2011) and McLaughlin *et al.* (2011b) and references therein.

The equilibrium magnetic field structure is taken as a simple 2D X-type neutral point:

$$\mathbf{B}_0 = B_0\left(\frac{x}{L},0,-\frac{z}{L}\right), \tag{2}$$

where B_0 is a characteristic field strength and L is the length scale for magnetic field variations. This magnetic field can be seen in Figure 1. Note that this particular choice of magnetic field is only valid in the neighbourhood of the null point located at $x = z = 0$. In addition, equation (2) is potential, although in general coronal fields are twisted and thus a potential field is a coarse approximation. We can also write $\mathbf{B}_0 = \nabla\times\mathbf{A}$ where $\mathbf{A} = (0, A_0, 0)$ is the vector potential. For our particular choice of equilibrium magnetic field, $A_0 = -xz$.

2.1 Linearised equations

To study the nature of wave propagation near null points, the linearised MHD equations are used. Using subscripts of 0 for equilibrium quantities and 1 for perturbed quantities, the linearised ver-

sions of equations (1) are:

$$\begin{aligned} \rho_0 \frac{\partial \mathbf{v}_1}{\partial t} &= \frac{1}{\mu}(\nabla \times \mathbf{B}_1) \times \mathbf{B}_0 \,, \\ \frac{\partial \mathbf{B}_1}{\partial t} &= \nabla \times (\mathbf{v}_1 \times \mathbf{B}_0) + \eta \nabla^2 \mathbf{B}_1 \,, \\ \frac{\partial \rho_1}{\partial t} + \nabla \cdot (\rho_0 \mathbf{v}_1) &= 0 \,, \qquad \nabla \cdot \mathbf{B}_1 = 0 \,. \end{aligned} \tag{3}$$

We will not discuss the linearised continuity equation further as it can be solved once we know $\mathbf{v}_1$. In fact, it has no influence on the momentum equation (in the low β approximation) and so in effect the plasma is arbitrarily compressible (e.g. Craig & Watson 1992).

We now consider a change of scale to non-dimensionalise; let $\mathrm{v}_1 = \bar{\mathrm{v}}\mathbf{w}_1^*$, $\mathbf{B}_0 = B_0\mathbf{B}_0^*$, $\mathbf{B}_1 = B_0\mathbf{B}_1^*$, $x = \underline{L}\,x^*$, $z = Lz^*$, $\nabla = \frac{1}{L}\nabla^*$ and $t = \bar{t}t^*$, where we let * denote a dimensionless quantity and $\bar{\mathrm{v}}, B_0$, L and $\bar{t}$ are constants with the dimensions of the variable they are scaling. We then set $B_0/\sqrt{\mu\rho_0} = \bar{\mathrm{v}}$ and $\bar{\mathrm{v}} = a/\bar{t}$ (this sets $\bar{\mathrm{v}}$ as the background Alfvén speed). This process non-dimensionalises equations (3) and under these scalings, $t^* = 1$ (for example) refers to $t = \bar{t} = L/\bar{\mathrm{v}}$; i.e. the (background) Alfvén time taken to travel a distance L. For the rest of this paper, we drop the star indices; the fact that they are now non-dimensionalised is understood.

We now restrict our attention to 2.5D MHD, i.e. 3D MHD with an invariant direction, and here we arbitrarily take $\partial/\partial y = 0$. In addition, from now on we consider an ideal plasma (i.e. let $\eta = 0$ or $R_m \to \infty$) but will discuss the role of resistivity further in the conclusions. Numerical diffusion, although present in all numerical simulations, plays a negligible role. The linearised MHD equations (3) naturally decouple into two sets of equations, with one set governing the behaviour in the invariant direction (i.e. here the $y-$direction) and the other governing behaviour in the $xz-$plane only. Furthermore, McLaughlin & Hood (2004) showed that the behaviour in the invariant direction corresponded to Alfvén wave behaviour, and that the equations in the $xz-$plane governed the fast MHD wave behaviour (note the slow MHD wave is absent in the low-β limit).

In this paper, we focus on the linearised equations for the Alfvén wave, with $\mathbf{v}_1 = (v_x, v_y, v_z)$ and $\mathbf{B}_1 = (b_x, b_y, b_z)$. For details of the fast wave equations see the review by McLaughlin *et al.* (2011a). The equations governing the behaviour in the invariant direction (i.e. the $y-$direction) are:

$$\begin{aligned} \rho_0 \frac{\partial v_y}{\partial t} &= (\mathbf{B}_0 \cdot \nabla) b_y = \left(B_x \frac{\partial}{\partial x} + B_z \frac{\partial}{\partial z} \right) b_y \,, \\ \frac{\partial b_y}{\partial t} &= (\mathbf{B}_0 \cdot \nabla) v_y + \frac{1}{R_m}\nabla^2 b_y = \left(B_x \frac{\partial}{\partial x} + B_z \frac{\partial}{\partial z} \right) v_y + \frac{1}{R_m}\left(\frac{\partial^2}{\partial x^2} + \frac{\partial^2}{\partial z^2} \right) b_y \,, \end{aligned} \tag{4}$$

where v_y is the velocity out of the plane that $\mathbf{B}_0$ defines. Hence, waves with this velocity will be *transverse* waves (energy flow perpendicular to the wavevector).

We will now vary the background plasma density. A straightforward way to add a non-uniform density profile to the governing equations is to consider $\rho_0 = \rho_0(A_0)$, where $\mathbf{A} = (0, A_0, 0)$ is the vector potential and A_0 is its $y-$coordinate. Thus, since ∇A_0 is perpendicular to $\mathbf{B}_0$, we have a density gradient perpendicular to the magnetic field. Under this model, ρ_0 is now constant *along* a fieldline but it can vary *across* fieldlines, i.e. vary from fieldline to fieldline. Hence, the equilibrium density is purely a function of A_0, namely

$$\rho_0 = \rho_0(A_0) = \rho_0(xz) \,, \tag{5}$$

where $A_0 = -xz$ (recall that at this point all our variables are non-dimensionalised). Thus equations (4) can be combined and written as:

$$\frac{\partial^2 v_y}{\partial t^2} = \frac{1}{\rho_0(xz)} (\mathbf{B}_0 \cdot \nabla)^2 v_y = \frac{1}{\rho_0(xz)} \left(B_x \frac{\partial}{\partial x} + B_z \frac{\partial}{\partial z} \right)^2 v_y = \frac{1}{\rho_0(xz)} \left(x \frac{\partial}{\partial x} - z \frac{\partial}{\partial z} \right)^2 v_y \,, \tag{6}$$

where we have taken $\eta = 0$ and have implemented our choice of $\mathbf{B}_0$ from equation (2).
This is the primary equation we will be utilising in this paper to investigate the behaviour of the Alfvén wave. In its derivation, we have assumed linearised behaviour in an ideal 2.5D plasma, i.e. a 3D plasma with an invariant direction.
If we now define $V_{A0}(xz) = 1/\sqrt{\rho_0(xz)}$ then equation (6) can be written as:

$$\frac{\partial^2 v_y}{\partial t^2} = V_{A0}(xz)^2 \left(x \frac{\partial}{\partial x} - z \frac{\partial}{\partial z} \right)^2 v_y = V_{A0}(xz)^2 (\mathbf{B}_0 \cdot \nabla)^2 v_y \tag{7}$$

Here $V_{A0}(xz)$ is related to the equilibrium (Alfvén) speed of the system. It is precisely this non-constant Alfvén speed, i.e. $V_{A0} = V_{A0}(xz)$, that leads to gradients in the Alfvén-speed profile, and hence to the possibility of phase mixing. Note that ρ_0 was assumed to be constant (i.e. $V^*_{A0} = 1$) in the models of McLaughlin & Hood (2004; 2005; etc) and there was no possibility of phase mixing, i.e. we have now removed a key assumption of these previous models.

2.2 Method of Characteristics and D'Alembert solution

Equation (7) can be solved using the method of characteristics. Let $\frac{d}{ds} = \mathbf{B}_0 \cdot \nabla = x\frac{\partial}{\partial x} - z\frac{\partial}{\partial z}$, where s is a parameter along a characteristic, and compare with, e.g., $\frac{dv_y}{ds} = \frac{dx}{ds}\frac{\partial v_y}{\partial x} + \frac{dz}{ds}\frac{\partial v_y}{\partial z}$. Comparing like terms yields:

$$x = x_0 e^s \,, \quad z = z_0 e^{-s} \,, \tag{8}$$

where x_0 and z_0 are the starting positions of our characteristics. Thus, $s = -\log\frac{z}{z_0} = \log\frac{x}{x_0}$. Thus equation (7) can be written:

$$\frac{\partial^2 v_y}{\partial t^2} = \frac{1}{\rho_0(xz)} \frac{d^2}{ds^2} v_y = V_{A0}^2 \frac{d^2}{ds^2} v_y \,. \tag{9}$$

This characteristic equation can be solved with a D'Alembert solution such that:

$$v_y = \mathscr{F}\left[t - \sqrt{\rho_0}\, s\right] + \mathscr{G}\left[t + \sqrt{\rho_0}\, s\right] = \mathscr{F}\left[t - \frac{s}{V_{A0}(A_0)}\right] + \mathscr{G}\left[t + \frac{s}{V_{A0}(A_0)}\right] \tag{10}$$

where $\mathscr{F}$ and $\mathscr{G}$ are functions prescribed by the initial/boundary conditions. Note here that we can only implement the D'Alembert solution since A_0 is a constant along each fieldline (characteristic).

2.3 Equilibrium density profiles

In this paper, we are investigating the effect of including a non-uniform background density profile, and we present results from four scenarios. The first three cases will consider a density profile of the form $\rho_0 = 1 + \lambda (xz)^2$, where we vary the parameter λ. Firstly, we will consider a uniform density profile (where $\lambda = 0$). This system is identical to that investigated in McLaughlin & Hood

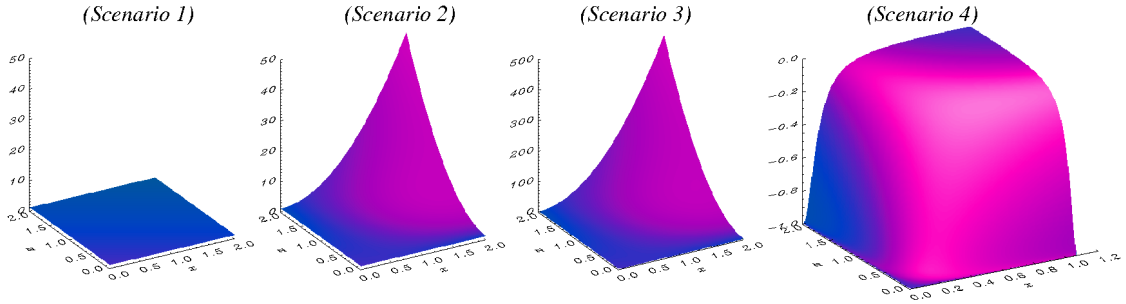

Figure 2: *Scenario 1* shows density profile of scenario 1, i.e. $\rho_0 = 1$ (uniform density). *Scenario 2* shows density profile of scenario 2, i.e. $\rho_0 = 1 + 3(xz)^2$ (weakly non-uniform density). *Scenario 3* shows density profile of scenario 3, i.e. $\rho_0 = 1 + 30(xz)^2$ (strongly non-uniform density, note change in $z-$axis). *Scenario 4* shows density profile of scenario 4, i.e. $\rho_0 = [1 + 30(xz)^2]^{-1}$. Since $0 < \rho_0 \leq 1$ in scenario 4, this subfigure is presented as a surface of $-\rho_0$, as this shows the profile behaviour more clearly.

(2004), and provides an excellent visual comparison to the other scenarios. Secondly, we consider a weakly changing density profile of the form $\rho_0 = 1 + 3(xz)^2$ ($\lambda = 3$) and thirdly, we consider a more extreme density profile of the form $\rho_0 = 1 + 30(xz)^2$ ($\lambda = 30$). The second and third choices of density profile consider a region of highest V_{A0}, i.e. smallest ρ_0 *close to the null point*. We will also consider a fourth scenario where $\rho_0 = [1 + 30(xz)^2]^{-1}$, where the maximum V_{A0} now occurs *away* from the null point. Tests show that these four choices of density profile communicate all the general results well. These four density profiles can be seen in Figure 2 (note the axes vary between subfigures).

3 Numerical Simulations & Analytical Solutions

In this section, we solve equations (4) numerically using a two-step Lax-Wendroff scheme and we present results from four non-uniform density scenarios. We drive our system with a wave pulse along the entire upper boundary, and we present a computational domain ($0 \leq x \leq 2$, $0 \leq z \leq 2$) with a single wave pulse coming in across the top boundary ($x = 2$). The boundary conditions were set such that:

$$v_y(x,2,t) = \sin(\omega t) \quad \text{for} \quad \begin{cases} 0 \leq x \leq 2 \\ 0 \leq t \leq \frac{\pi}{\omega} \end{cases} \quad ,$$
$$v_y = 0 \qquad \text{otherwise}$$
$$\left.\frac{\partial v_y}{\partial x}\right|_{x=2} = 0\,, \qquad \left.\frac{\partial v_y}{\partial x}\right|_{x=0} = 0\,, \qquad \left.\frac{\partial v_y}{\partial z}\right|_{z=0} = 0\,. \tag{11}$$

Results presented in this paper have a typical numerical resolution of 2000×2000 and (successful) convergence tests were performed. As detailed in §2.2, the governing Alfvén wave equations can also be solved analytically (i.e. using equation 10). In order to compare the analytical and numerical results, we must substitute the same initial conditions into the D'Alembert solution, i.e. $\mathscr{F}(t) =$

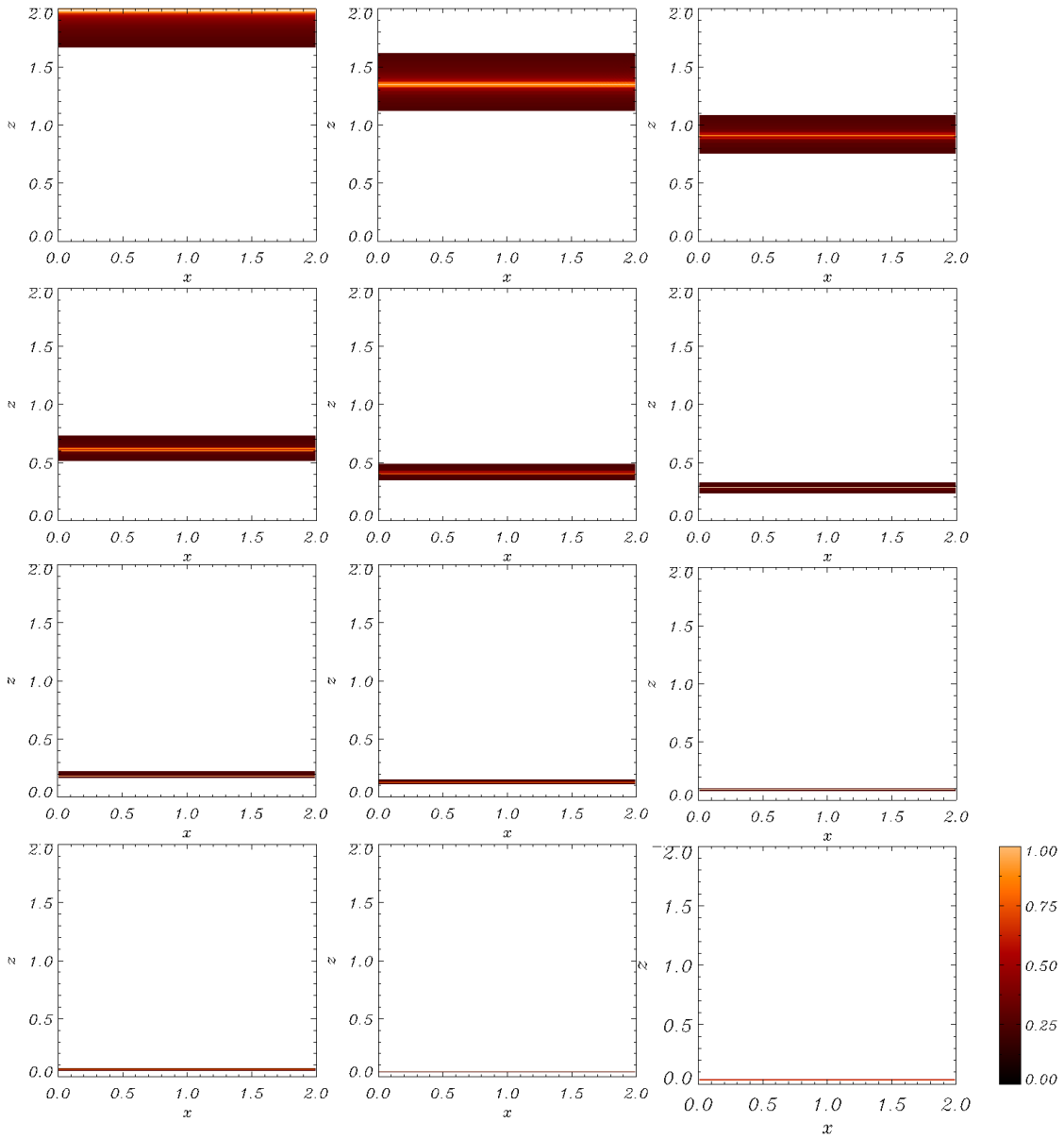

Figure 3: Contours of v_y for an Alfvén wave sent in from upper boundary for $0 \leq x \leq 2$ and its resultant propagation at times (a) t=0.25, (b) t=0.6, (c) t=1.0, (d) $t = 1.4$, (e) t=1.8, (f) t=2.2, (g) $t = 2.6$, (h) t=3.0, (i) t=3.4, (j) $t = 3.8$, (k) t=4.2, (l) t=4.6, labelling from top left to bottom right.

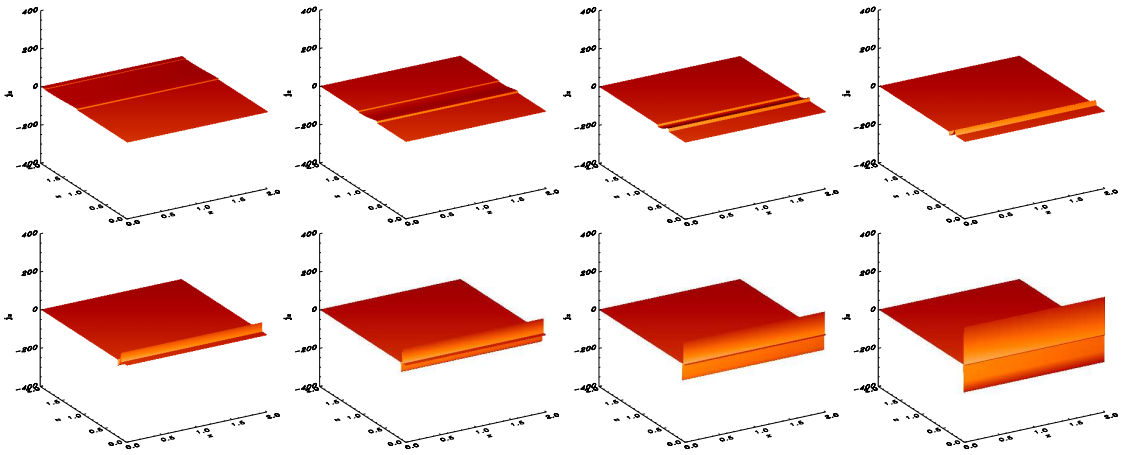

Figure 4: Shaded surfaces showing the build-up of j_x at times (a) t=0.5, (b) t=1.0, (c) t=1.5, (d) t=2.0, (e) t=2.5, (f) t=3.0, (g) t=3.5 and (h) t=4.0, labelling from top left to bottom right.

$\sin(\omega t)$ to get the analytical solution for v_y, namely:

$$v_y(x,z,t) = \sin\omega\left(t+\sqrt{\rho_0(xz)}\log\frac{z}{z_0}\right) \quad \text{for} \quad \begin{cases} 0 \le t+\sqrt{\rho_0(xz)}\log\frac{z}{z_0} \le \frac{\pi}{\omega} \\ 0 \le x_0 \le 2 \end{cases} . \tag{12}$$

It should also be noted that the agreement between all the numerical and analytical work in this paper is excellent.

We can also use our D'Alembert solution to calculate b_y and hence j_x and j_z. For the first three scenarios; $\rho_0 = 1+\lambda(xz)^2$, and so using equation (12) we can write:

$$b_y = -\sqrt{1+\lambda x^2z^2}\sin\left[\omega\left(t+\sqrt{1+\lambda x^2z^2}\log\frac{z}{z_0}\right)\right], \tag{13}$$

$$\begin{aligned} j_x = {} & \left[\frac{\omega(1+\lambda x^2z^2)}{z}+\omega\lambda x^2 z\log\frac{z}{z_0}\right]\cos\left[\omega\left(t+\sqrt{1+\lambda x^2z^2}\log\frac{z}{z_0}\right)\right] \\ & +\frac{\lambda x^2 z}{\sqrt{1+\lambda x^2z^2}}\sin\left[\omega\left(t+\sqrt{1+\lambda x^2z^2}\log\frac{z}{z_0}\right)\right] \end{aligned} \tag{14}$$

$$\begin{aligned} j_z = {} & -\frac{\lambda xz^2}{\sqrt{1+\lambda x^2z^2}}\sin\left[\omega\left(t+\sqrt{1+\lambda x^2z^2}\log\frac{z}{z_0}\right)\right] \\ & -\omega\log\left(\frac{z}{z_0}\right)\lambda xz^2\cos\left[\omega\left(t+\sqrt{1+\lambda x^2z^2}\log\frac{z}{z_0}\right)\right] \end{aligned} \tag{15}$$

Note that the analytical solution for b_y, j_x and j_z is slightly different for $\rho_0 = 1/[1+30(xz)^2]$.

3.1 Scenario 1 : Uniform Density ($\lambda = 0$)

The first three scenarios will consider a density profile of the form $\rho_0 = 1+\lambda(xz)^2$, where we vary the parameter λ. Firstly, we will consider a uniform density profile (where $\lambda = 0$). The resultant wave evolution can be seen in Figure 3.

We find that the linear Alfvén wave propagates downwards from the top boundary and begins to spread out, following the fieldlines. As the wave approaches the $x-$axis (the separatrix), it thins

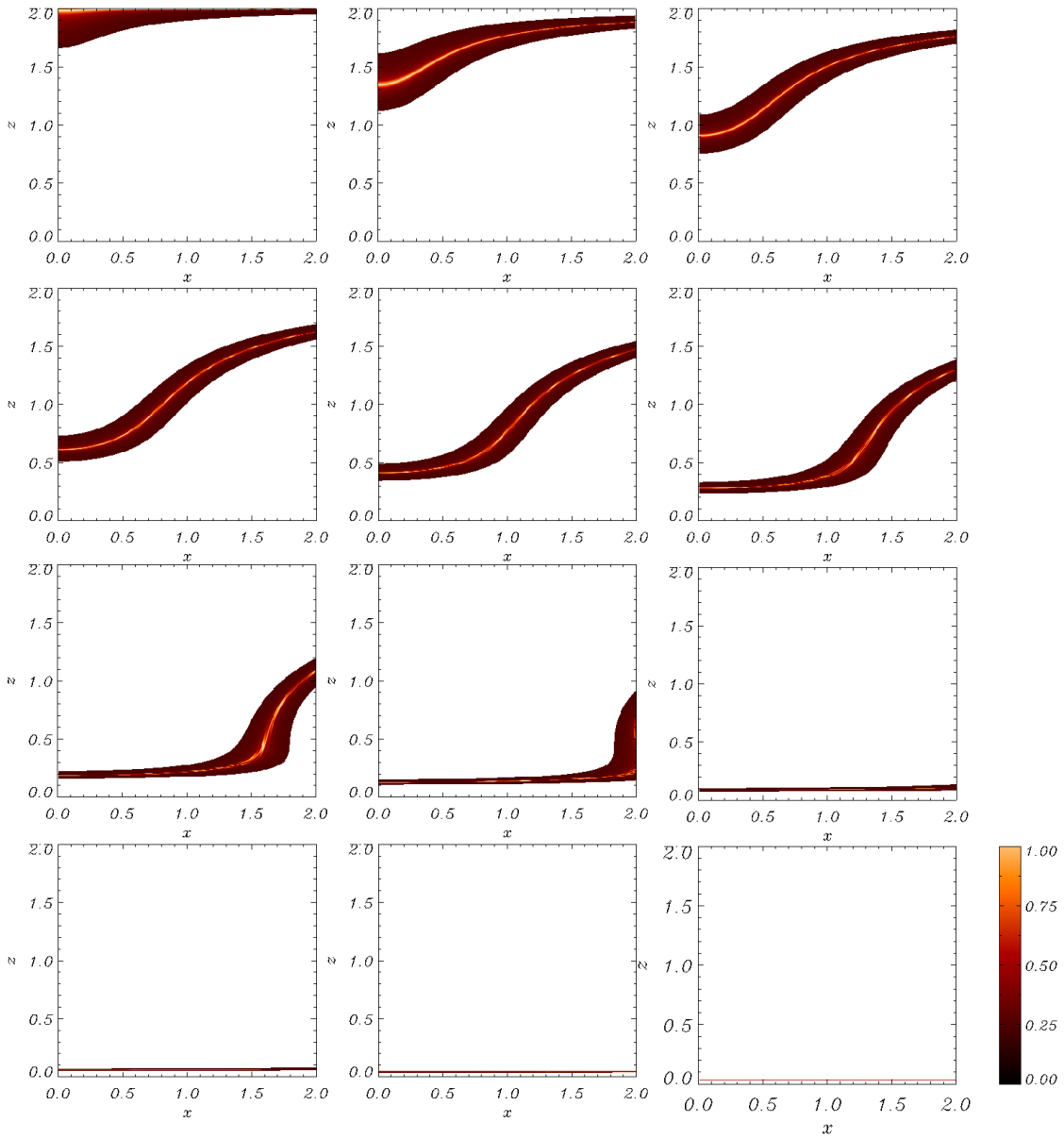

Figure 5: Contours of v_y for an Alfvén wave sent in from upper boundary for $0 \leq x \leq 2$ and its resultant propagation at times (a) t=0.25, (b) t=0.6, (c) t=1.0, (d) $t = 1.4$, (e) t=1.8, (f) t=2.2, (g) $t = 2.6$, (h) t=3.0, (i) t=3.4, (j) $t = 3.8$, (k) t=4.2, (l) t=4.6, labelling from top left to bottom right.

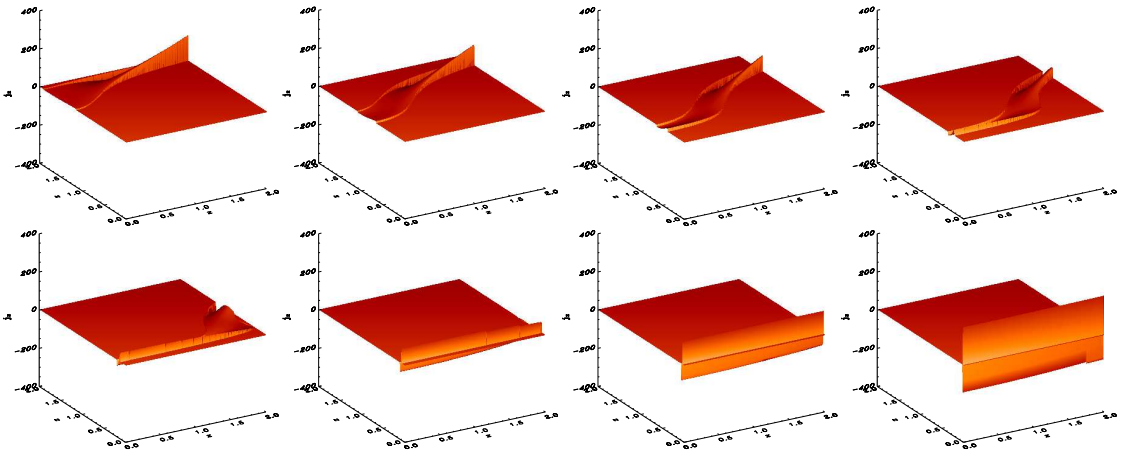

Figure 6: Shaded surfaces showing the build-up of j_x at times (a) t=0.5, (b) t=1.0, (c) t=1.5, (d) t=2.0, (e) t=2.5, (f) t=3.0, (g) t=3.5 and (h) t=4.0, labelling from top left to bottom right.

but keeps its original amplitude. The wave eventually accumulates very near the separatrix. Note that these results are similar to those investigated in McLaughlin & Hood (2004), and are presented here to provide a visual comparison and contrast to the other scenarios (McLaughlin & Hood 2004 actually used a different driver, making direct comparisons with scenarios 2, 3 & 4 less obvious).

We can also solve equation (6) using our D'Alembert solution. Here, equations (13 - 15) can be simplified under $\lambda = 0$ to give:

$$b_y = -\sin\omega\left(t + \log\frac{z}{z_0}\right) \ , \ \ j_x = \frac{\omega}{z}\cos\omega\left(t + \log\frac{z}{z_0}\right) \ , \ \ j_z = 0 \ .$$

Hence, the Alfvén wave causes current density to build up along the separatrix. Furthermore, since $z = z_0 e^{-s}$ from equation (8), we see that this j_x build up is *exponential* in time (due to the $1/z$ dependence) whereas $j_z = 0$ for all time. Figure 4 shows the build-up of j_x.

3.2 Scenario 2 : Weakly non-uniform Density ($\lambda = 3$)

We now consider a weakly non-uniform density profile: $\rho_0(x,z) = 1 + 3x^2z^2$. As in scenario 1 in §3.1, equations (4) are solved numerically using our two-step Lax-Wendroff scheme, utilising the same boundary and initial conditions (equations 11) but now implementing our weakly-changing density profile, i.e. the governing Alfvén wave equation is now:

$$\frac{\partial^2 v_y}{\partial t^2} = \frac{1}{1+3x^2z^2}\left(x\frac{\partial}{\partial x} - z\frac{\partial}{\partial z}\right)^2 v_y \ .$$

The results for v_y can be seen in Figure 5. We see that the Alfvén wave again descends from the upper boundary ($x = 2$) and accumulates along the separatrix ($x-$axis), but now the (initially planar) wave is distorted; a phenomenon not seen in previous null point studies. The varying speed, $V_{A_0}(xz)$, means different fluid elements of the wave travel at different speeds. Thus, the fluid elements of the wave closest to the $x = 0$ axis, where $V_{A_0}(xz)$ takes its maximum value (or alternatively $\rho_0(xz)$ takes its minimum value) propagate at a greater speed than those fluid elements away from the axis (i.e. left-hand-side propagates faster than right). Thus, the wave is distorted and descends at different

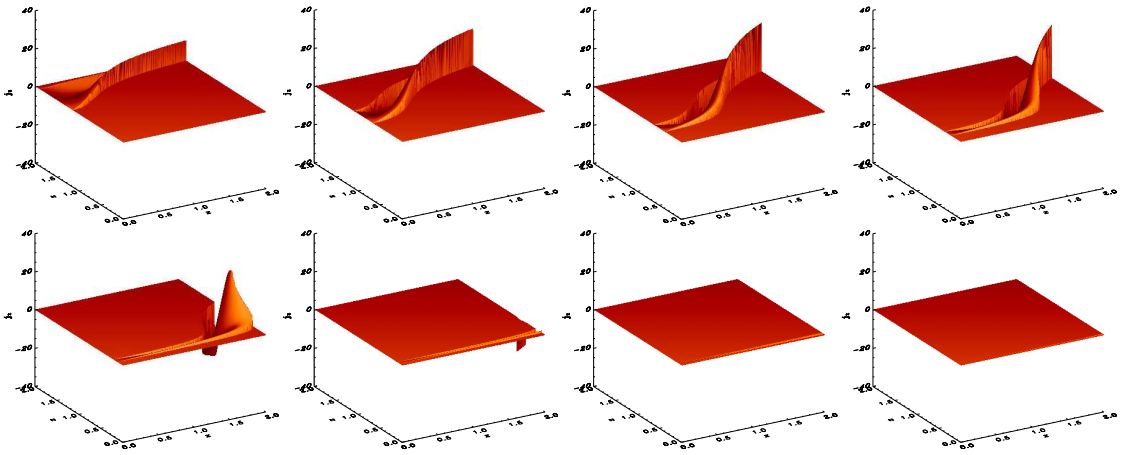

Figure 7: Shaded surfaces showing the build-up of j_z at times (a) t=0.5, (b) t=1.0, (c) t=1.5, (d) t=2.0, (e) t=2.5, (f) t=3.0, (g) t=3.5 and (h) t=4.0, labelling from top left to bottom right.

rates. This is clearly significantly different wave behaviour to that of the uniform density case considered in Figure 3. The wave does however still eventually accumulate along the separatrix.

Again, the D'Alembert solution agrees exactly with the numerical simulation. Substituting $\lambda = 3$ into equations (14) and (15) gives analytical forms for j_x and j_z. These can be seen in Figures 6 and 7, respectively. In Figure 6, we can see that there is a large concentration of j_x initially along the wave, due to the changing density profile. This concentration propagates with the wave and begins to accumulate along the separatrix ($x-$axis). The build-up of j_x along the separatrix is substantially more than in early subfigures. In Figure 7, we can see that there is initially a concentration of j_z (due to the changing density profile) but that this decays away as time elapses. Hence the separatrix is still be the location for preferential heating due to Alfvén waves, even with the inclusion of a (weakly) non-uniform density profile.

3.3 Scenario 3 : Strongly non-uniform Density ($\lambda = 30$)

We now consider a strongly non-uniform density profile: $\rho_0(x,z) = 1 + 30x^2z^2$. As in scenarios 1 & 2 above, equations (4) are solved numerically using a two-step Lax-Wendroff scheme, utilising the same boundary and initial conditions (equations 11) but now implementing our strongly-changing density profile, i.e. the governing Alfvén wave equation is now:

$$\frac{\partial^2 v_y}{\partial t^2} = \frac{1}{1+30x^2z^2}\left(x\frac{\partial}{\partial x} - z\frac{\partial}{\partial z}\right)^2 v_y \, .$$

The resultant propagation of v_y can be seen in Figure 8. The Alfvén wave behaviour is similar to that seen for the weakly-changing density profile (§3.2), but with one important distinction. Again, we see that the Alfvén wave descends and accumulates along the separatrix. The wave is distorted from its original planar form by the varying density profile, and hence different parts of the wave descend at different speeds. Thus, the wave travels faster nearer to the $z-$axis than away from it. However, since the Alfvén wave is confined to the fieldlines, and propagating along those fieldlines, there comes a point where fluid elements of the wave are so ahead of other elements of the wave that the wavefront (made by joining up all the elements at the same s value) actually bends back

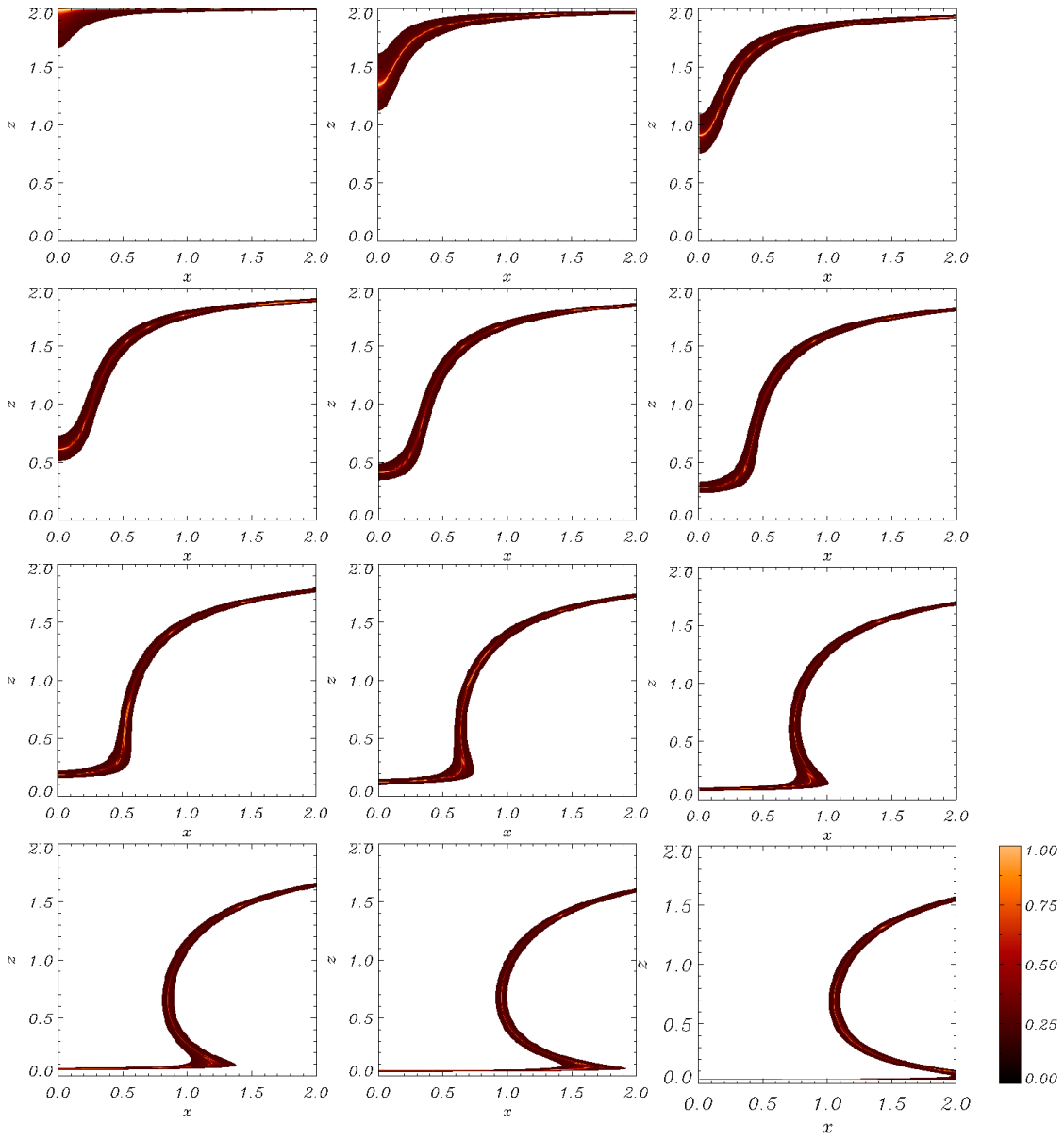

Figure 8: Contours of v_y for an Alfvén wave sent in from upper boundary for $0 \leq x \leq 2$ and its resultant propagation at times (a) t=0.25, (b) t=0.6, (c) t=1.0, (d) $t = 1.4$, (e) t=1.8, (f) t=2.2, (g) $t = 2.6$, (h) t=3.0, (i) t=3.4, (j) $t = 3.8$, (k) t=4.2, (l) t=4.6, labelling from top left to bottom right.

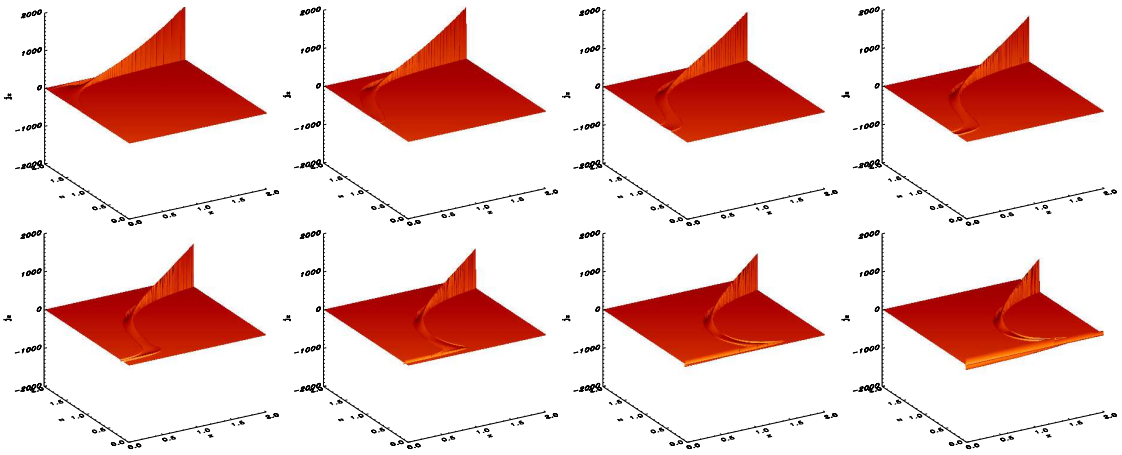

Figure 9: Shaded surfaces showing the build-up of j_x at times (a) t=0.5, (b) t=1.0, (c) t=1.5, (d) t=2.0, (e) t=2.5, (f) t=3.0, (g) t=3.5 and (h) t=4.0, labelling from top left to bottom right.

upon itself; again a phenomenon not seen before in null point investigations. This can be seen most clearly in the lower subfigures of Figure 8. Despite this however, once again the Alfvén wave still eventually accumulate along the separatrix ($x-$axis).

Since the wave is so stretched where it forms the 'reflection point' in the wavefront, there may be a great deal of current build-up near this point. Hence, this may provide an additional location for (preferential) heating, and so we investigate the resultant j_x and j_z.

As before, the D'Alembert solution agrees exactly with the numerical simulation. Substituting $\lambda = 30$ into equations (14) and (15) gives analytical forms for j_x and j_z, and these can be seen in Figures 9 and 10. In Figure 9, we can see that there is indeed a very large concentration (note value on axis!) of j_x initially along the wave, due to the changing density profile. This current concentration propagates co-spatially with the wave and begins to accumulate along the separatrix ($x-$axis). This build-up along the separatrix eventually overtakes the magnitude of current concentrations elsewhere (although this occurs at a later time than that shown in the last subfigure). Hence, the separatrix will *still* be the location for the majority of heating, however small η is taken to be. Of course, if η is taken to be extremely large (unphysical) then there may be some heating along other parts of the Alfvén wave. However, the density profile invoked in this scenario has a very extreme distribution and so perhaps under coronal conditions this scenario would not take place and, consequently, preferential heating would *still occur along the separatrices*.

In Figure 10, we can see that there is initially a concentration of j_z (due to the changing density profile). This propagates in the increasing x and decreasing z directions, and decays away near the $x-$axis. The rest of the j_z concentration propagates away and out of our box, but will eventually decay away (like j_z did before). This can be see in the form of j_z from equations (15).

It is perhaps not clear from Figures 9 and 10 alone that the maximum current build-up (still) occurs at the $x-$axis ($z = 0$ line). To show this analytically, we can utilise equations (14) and (15) in combination with equations (8). Thus, we can substitute $x = x_0 e^s$, $z = z_0 e^{-s}$ and hence $xz = x_0 z_0$ to

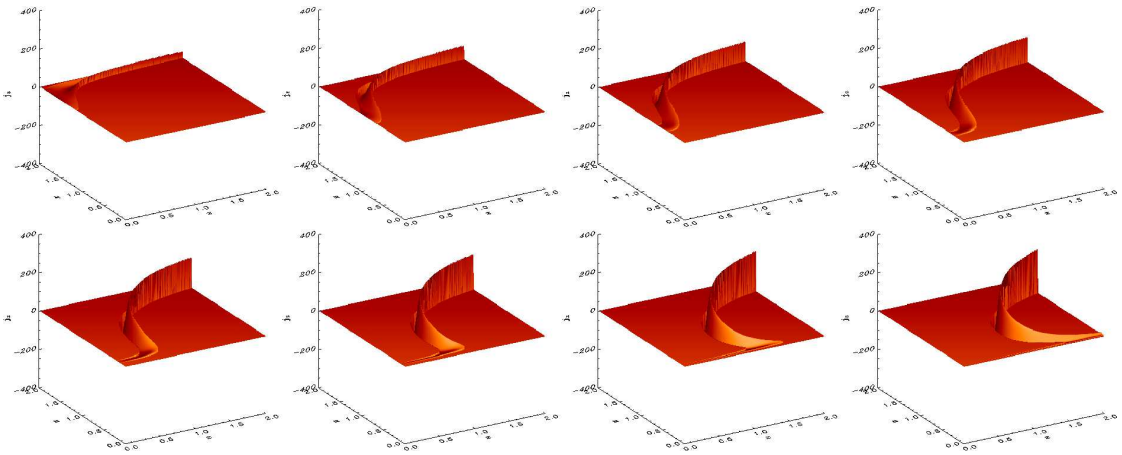

Figure 10: Shaded surfaces showing the build-up of j_z at times (a) t=0.5, (b) t=1.0, (c) t=1.5, (d) t=2.0, (e) t=2.5, (f) t=3.0, (g) t=3.5 and (h) t=4.0, labelling from top left to bottom right.

give:

$$\begin{aligned} j_x &= e^s \left\{ \left[\frac{\omega\rho_0}{z_0} - (\omega\lambda x_0^2 z_0)\, s \right] \cos\omega\,(t-\sqrt{\rho_0}s) + \frac{\lambda x_0^2 z_0}{\sqrt{\rho_0}} \sin\omega\,(t-\sqrt{\rho_0}s) \right\} \\ &= e^s\,[(B-Cs)\cos\omega\,(t-\sqrt{\rho_0}s) + D\sin\omega\,(t-\sqrt{\rho_0}s)] \\ j_z &= e^{-s} \left[-\frac{\lambda x_0 z_0^2}{\sqrt{\rho_0}} \sin\omega\,(t-\sqrt{\rho_0}s) + (\omega\lambda x_0 z_0^2)\, s\cos\omega\,(t-\sqrt{\rho_0}s) \right] \\ &= e^{-s}\,[-E\sin\omega\,(t-\sqrt{\rho_0}s) + F\,s\cos\omega\,(t-\sqrt{\rho_0}s)] \end{aligned} \tag{16}$$

where x_0, z_0, ω, λ, ρ_0, B, C, D, E and F are all constants for a specific fieldline (B,...,F are just collected constants but are all strictly positive).

Figure 11 shows a surface of the build-up of j_x plotted against z and time, along $x = 0.5$. Here, we can see that z decreases from $z = 2$ down to near $z = 0$ as time elapses and that j_x is building up the closer we are to $z = 0$ and the build-up is increasing in time.

Hence, we can see now clearly see that the behaviour of j_x and j_z follow complicated forms that depend upon many starting parameters and on s, but that at large times, j_x will eventually build-up exponentially and j_z will decay exponentially. Thus, for the linear Alfvén wave, preferential heating will still occur along the separatrices, despite the inclusion of either weakly or strongly non-uniform density profiles.

3.4 Scenario 4 : Non-uniform Density $\rho_0 = [1 + 30\,(xz)^2]^{-1}$

We now consider our final non-uniform density profile: $\rho_0 = [1 + 30\,(xz)^2]^{-1}$. As before, equations (4) are solved numerically using a two-step Lax-Wendroff scheme, with the same boundary and initial conditions (given by equations 11) but now implementing our fourth non-uniform density profile. Thus, the governing Alfvén wave equation is now:

$$\frac{\partial^2 v_y}{\partial t^2} = (1 + 30x^2z^2) \left(x\frac{\partial}{\partial x} - z\frac{\partial}{\partial z} \right)^2 v_y \,.$$

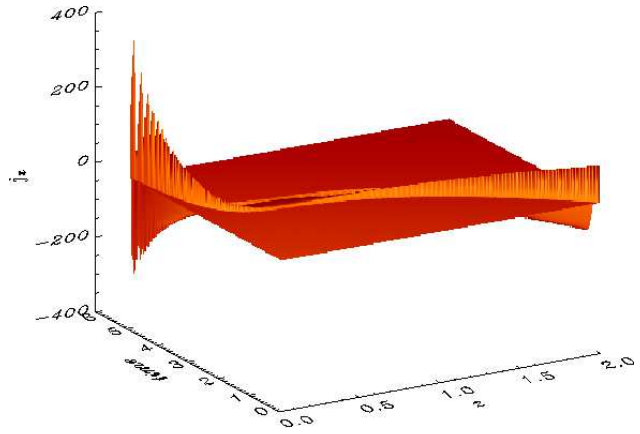

Figure 11: Shaded surfaces showing the build-up of j_x plotted against z and time with $x = 0.5$.

The results for v_y can be seen in Figure 12. Here, the greatest magnitude of V_{A_0} occurs away from the axes (in these numerical boxes the maximum occurs at $x = z = 2$). Thus, we find that the Alfvén wave is again distorted from its initially planar shape, but that it now travels faster the *further* we are away from the null point / axes. The first subfigure of Figure 12 shows the massive speed differential across the wave after a very short time. The linear Alfvén wave then descends and starts to accumulate along the $x-$axis (separatrix). Here, the wave slows down and thins, but keeps its original amplitude. There is no spike / reflection point formed, as there was in §3.3. This is clearly a different velocity profile to that seen in the previous three figures (i.e. Figs 3, 5 & 9) but the phenomenon of different fluid elements propagating at different speeds due to the non-uniform density profile is common to all scenarios.

As before, the D'Alembert solution agrees exactly with the numerical simulation, and we can use our D'Alembert solution to work out b_y, j_x and j_z (as we did in equations 13-15) for this fourth density profile. The resultant behaviour for j_x and j_z can be seen in Figures 13 and 14. In Figure 13, we can see that there is initially a large concentration of j_x due to the extreme density profile, but that this then decays away (as the wave propagates along the fieldlines and out of the box). At a later time, after the wave is near the separatrix, j_x starts to grow again. In Figure 14, we can see that there is initially a large concentration of j_z (due to the changing density profile), but that it very quickly decays away. Thus, there is a large current accumulation along the separatrix and our key result about preferential Alfvén wave heating again holds.

As mentioned above, our D'Alembert solution gives us general forms for b_y, j_x and j_z. Substituting $\rho_0 = [1+\gamma(xz)^2]^{-1}$ into these forms (where $\gamma = 30$ in this study case but γ is used so the result is more general) and substituting $xz = x_0 z_0$ and $x = x_0 e^s$, $z = z_0 e^{-s}$ gives:

$$\begin{aligned} j_x &= e^s\left[\left(\omega\gamma x_0^2 z_0^2 \rho_0\, s + \frac{\omega}{z_0}\right)\cos\omega\,(t-\sqrt{\rho_0}s) - \rho_0^{\frac{3}{2}}\gamma x_0^2 z_0 \sin\omega\,(t-\sqrt{\rho_0}s)\right] \\ &= e^s\left[(B\,s+C)\cos\omega\,(t-\sqrt{\rho_0}s) - D\sin\omega\,(t-\sqrt{\rho_0}s)\right] \\ j_z &= e^{-s}\left[-s\omega\gamma x_0 z_0^2 \rho_0^2\cos\omega\,(t-\sqrt{\rho_0}s) + \gamma x_0 z_0^2 \rho_0^{\frac{3}{2}}\sin\omega\,(t-\sqrt{\rho_0}s)\right] \\ &= e^{-s}\left[E\sin\omega\,(t-\sqrt{\rho_0}s) + F\,s\cos\omega\,(t-\sqrt{\rho_0}s)\right] \end{aligned}$$

where again x_0, z_0, ω, γ, ρ_0, B, C, D, E and F are all constants for a specific fieldline (B,...,F are

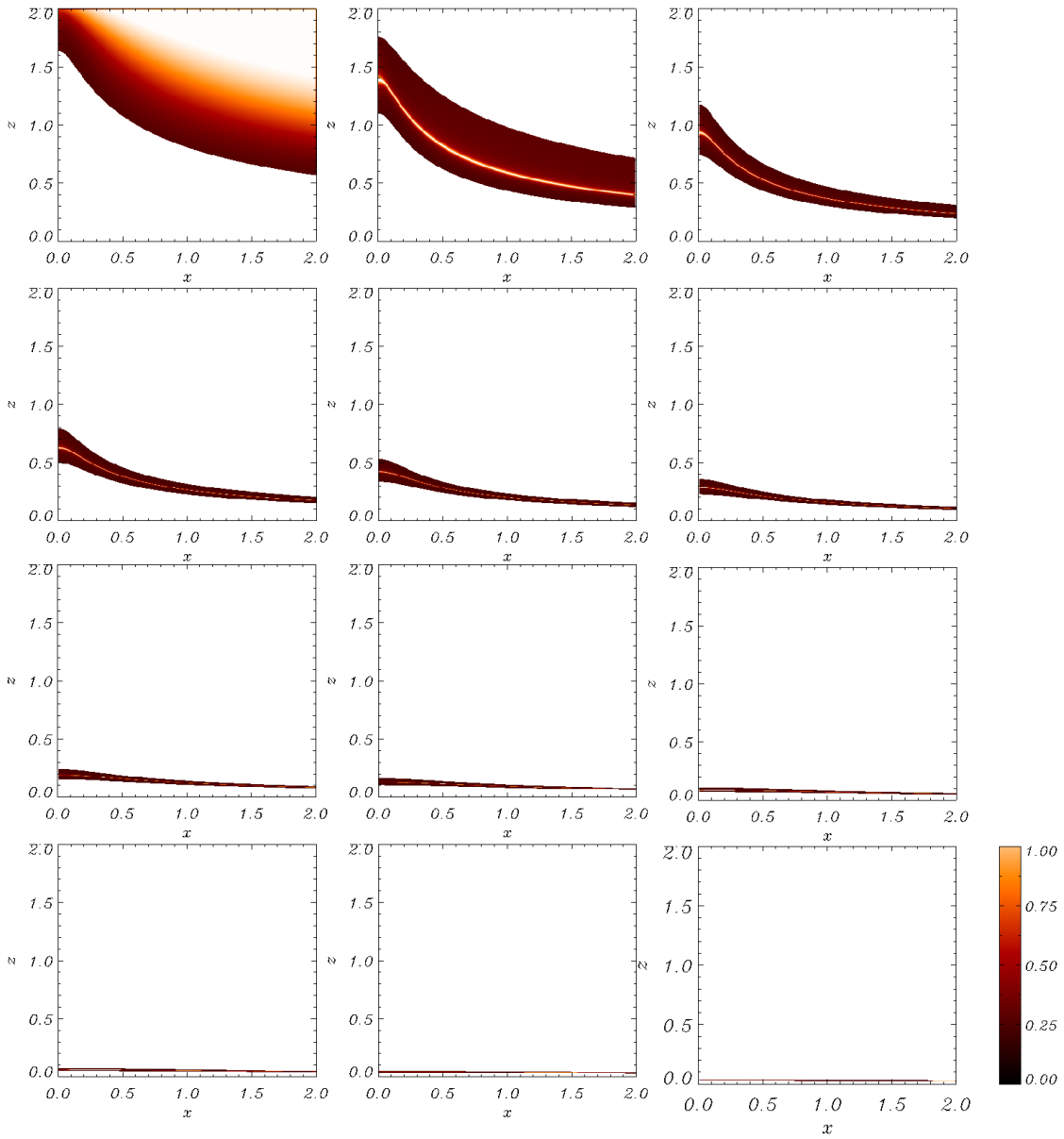

Figure 12: Contours of v_y for an Alfvén wave sent in from upper boundary for $0 \leq x \leq 2$ and its resultant propagation at times (a) t=0.25, (b) t=0.6, (c) t=1.0, (d) $t = 1.4$, (e) t=1.8, (f) t=2.2, (g) $t = 2.6$, (h) t=3.0, (i) t=3.4, (j) $t = 3.8$, (k) t=4.2, (l) t=4.6, labelling from top left to bottom right.

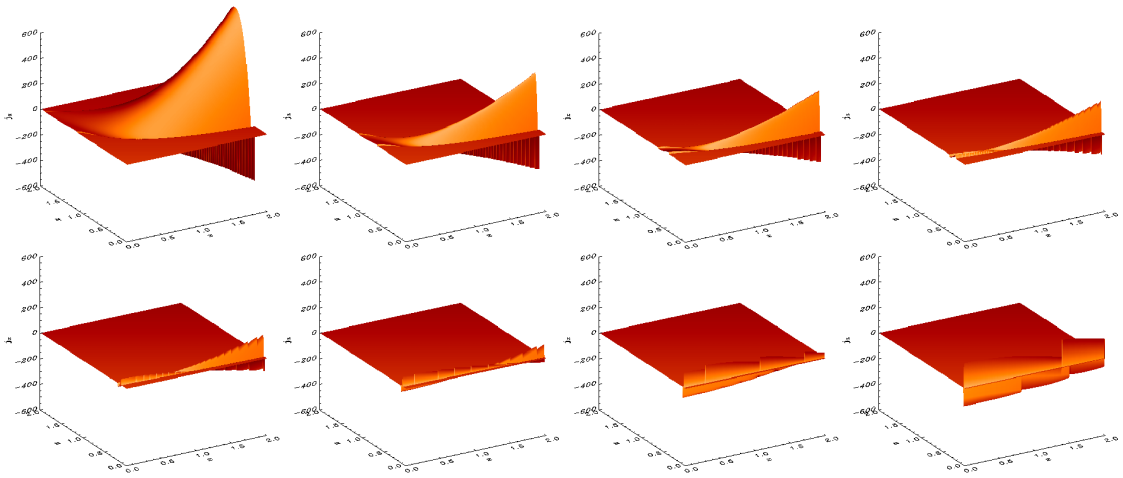

Figure 13: Shaded surfaces showing the build up of j_x at times (a) t=0.5, (b) t=1.0, (c) t=1.5, (d) t=2.0, (e) t=2.5, (f) t=3.0, (g) t=3.5 and (h) t=4.0, labelling from top left to bottom right.

just collected constants but are all strictly positive). Note that these equations have a similar form to equations (16) but the constants *B-F* are different.

Hence, we can see that the behaviour of j_x and j_z follow complicated forms that depend upon many starting parameters and on s, but that (as before) j_x will eventually build-up exponentially and j_z will decay exponentially. Thus, for the linear Alfvén wave, preferential heating will still occur along the separatrices, even when a non-uniform density profile is considered.

4 Conclusion

We have investigated the behaviour of the linear Alfvén wave in the neighbourhood of a 2D X-point geometry, investigating both uniform and non-uniform equilibrium density plasma. Specifically, we have considered four scenarios:

- Uniform Density: $\rho_0 =$constant
- Weakly non-uniform Density: $\rho_0 = 1 + 3x^2z^2$
- Strongly non-uniform Density: $\rho_0 = 1 + 30x^2z^2$
- Non-uniform Density: $\rho_0 = [1 + 30\,(xz)^2]^{-1}$

We find that the linear Alfvén wave propagates along the equilibrium fieldlines and a single wave-fluid element is confined to the fieldline that it starts on. Since the wave strictly follows the fieldlines, it spreads out as it approaches the diverging null point. When a uniform plasma density is considered, it was seen that the (initially planar) Alfvén wave front remains purely planar, despite the varying equilibrium Alfvén-speed profile, and that the current density accumulates *exponentially* at the separatrices. In the non-ideal case, these Alfvénic disturbances will dissipate their (wave) energy at these preferential locations.

We also investigated a variety of non-uniform equilibrium density profiles, and found that in these scenarios the (initially planar) wave front is now rapidly stretched and distorted. In fact, the wave-front is distorted from its initially planar shape and travels along the fieldlines at different speeds.

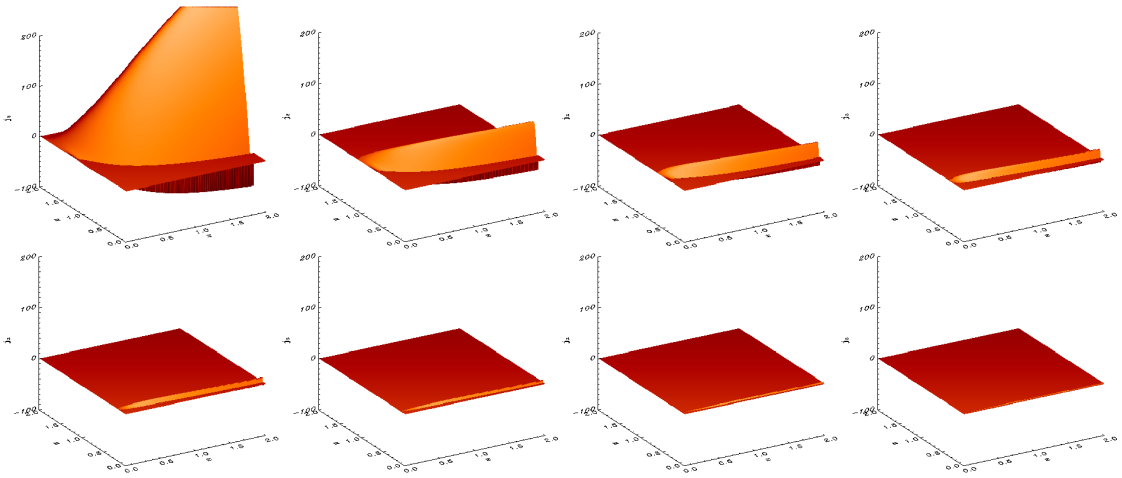

Figure 14: Shaded surfaces showing the build up of j_z at times (a) t=0.5, (b) t=1.0, (c) t=1.5, (d) t=2.0, (e) t=2.5, (f) t=3.0, (g) t=3.5 and (h) t=4.0, labelling from top left to bottom right.

Depending upon the exact form of the density profile, the wavefront can stretch so much that it bends back upon itself and creates a spike or 'reflection point' - an effect not reported before in the case of wave behaviour around null points. However, in some cases, the creation of such a reflection point can require an extreme and unphysical density profile.

This paper set out to answer a key question: with the addition of a non-uniform density, and thus removing one of the key restrictions of McLaughlin & Hood (2004) and subsequent papers, does the current density accumulation still occur preferentially at the separatrix or does phase mixing now allow the wave energy to be extracted from a different location? At its heart, the results in this paper have been all about the battle between *dissipation due to phase mixing* and *dissipation of the current build-up along the separatrices*. From our results above, we conclude that the current density build-up is limited except near the separatrices. Thus, our key result is that for the linear Alfvén wave preferential heating occurs along the separatrices, *even when a non-uniform density profile is considered*.

The energy carried by Alfvén waves is considered to play an important role in the heating of coronal holes and the acceleration of the solar wind (e.g. Ofman & Davila 1995; 1997; Chmielewski *et al.* 2013, and references therein). Our results highlight that the separatrices will be preferential locations for Alfvén wave heating and thus present a clear observational prediction.

Finally, this investigation has utilised linearised MHD equations (§2.1) and this approach is only valid when the perturbations in our physical parameters are much smaller than their equilibrium values. In addition, the Alfvén wave is slowing down as it approaches the separatrices, hence its gradients are increasing, and moreover these have been shown to grow exponentially (see §3.1, 3.2, 3.3 & 3.4). Thus, in a simple manner, our linearisation will start to break down on timescales $t \simeq -\log M_{\rm A}$, where $M_{\rm A}$ is the initial Alfvn Mach number. Thus, our results are valid for small-to-medium amplitude Alfvén waves, but further studies are required to fully understand the implications for large amplitude non-linear Alfvén waves.

Acknowledgements

The author acknowledges IDL support provided by STFC. JM wishes to thank Alan Hood for insightful discussions and constant encouragement.

References

Banerjee, D., Teriaca, L., Doyle, J. G. & Wilhelm, K., Astron. Astrophys., **339**, 208
Botha, G. J. J., Arber, T. D., Nakariakov, V. M., & Keenan, F. P., 2000, Astron. Astrophys., **363**, 1186
Bulanov, S. V., Syrovatskii, S. I., 1980, Fiz. Plazmy., **6**, 1205.
Chmielewski, P., Srivastava, A. K., Murawski, K. & Musielak, Z. E., 2013, MNRAS, **428**, 40
Close, R. M., Parnell, C. E. & Priest, E. R., 2004, Solar Phys., **225**, 21-46
Craig, I. J. D., McClymont, A. N., 1991, Astrophys. J., **371**, L41
Craig, I.J., Watson, P.G., 1992, Astrophys. J., **393**, 385-395.
Craig, I.J., McClymont, A.N., 1993, Astrophys. J., **405**, 207-215.
Dwivedi, B. N. & Srivastava, A. K., 2006, Solar Phys., **237**, 143
Erdélyi, R., Doyle, J. G., Perez, M. E. & Wilhelm, K., 1998, A&A, 337, 287
Galsgaard, K., Priest, E.R. & Titov, V.S., 2003, J. Geophys. Res. **108**, 1-12.
Galsgaard, K. & Pontin, D. I., 2011a, A&A, 529, A20
Galsgaard, K. & Pontin, D. I., 2011b, A&A, 534, A2
Harrison, R. A., Hood, A. W. & Pike, C. D. 2002, A&A, 392, 319
Hassam, A. B., 1992, Astrophys. J., **399**, 159-163.
Heyvaerts, J. & Priest, E. R., 1983, Astron. Astrophys., **117**, 220
Hood, A. W., Brooks, S. J. & Wright, A. N., 2002, Proc. Roy. Soc, **A458**, 2307
Kumar, D. & Bhattacharyya, R., 2011, Phys. Plasmas, **18**, 084506
Longcope, D. W., 2005, Living Rev. Solar Phys., **2**, http://www.livingreviews.org/lrsp-2005-7
Longcope, D. W. & Parnell, C. E., 2009, Solar Phys., **254**, 51
McLaughlin, J.A. & Hood, A.W., 2004, Astron. Astrophys. **420**, 1129
McLaughlin, J.A. & Hood, A.W., 2005, Astron. Astrophys. **435**, 313
McLaughlin, J.A. & Hood, A.W., 2006a, Astron. Astrophys. **452**, 603
McLaughlin, J.A. & Hood, A.W., 2006b, Astron. Astrophys. **459**, 641
McLaughlin, J.A., Ferguson, J. S. L. & Hood, A.W., 2008, Solar Phys. **251**, 563
McLaughlin, J.A., De Moortel, I., Hood, A.W. & Brady, C.S.: 2009, Astron. Astrophys. **493**, 227
McLaughlin, J. A., Hood, A. W. & De Moortel, I., 2011a, *Space Science Reviews*, **158**, 205
McLaughlin, J.A., De Moortel, I. & Hood, A.W., 2011b, Astron. Astrophys. **527**, A149
Ofman, L., Morrison, P. J. & Steinolfson, R. S., 1993, Astrophys. J., **417**, 748
Ofman, L., & Davila, J. M., 1995, J. Geophys. Res., **100**, 23413
Ofman, L., & Davila, J. M., 1997, Astrophys. J., **476**, 357
O'Shea, E., Banerjee, D. & Poedts, S., 2003, A&A, **400**, 1065
O'Shea, E., Banerjee, D. & Doyle, J. G., 2005, A&A, **436**, L35
Pontin, D.I., Galsgaard, K., 2007, J. Geophys. Res. **112**, 3103.
Pontin, D.I., Bhattacharjee, A., Galsgaard, K., 2007, *Phys. Plasmas* **14**, 2106.
Régnier, S., Parnell, C. E. & Haynes, A. L., 2008, Astron. Astrophys., **484**, L47
Steinolfson, R. S., Ofman, L. & Morrison, P. J., 1995, Space plasmas: coupling between small and medium scale processes, AGU, 189
Tomczyk, S., McIntosh, S. W., Keil, S. L., Judge, P. G., Schad, T., Seeley, D. H. & Edmondson, J., 2007, Science, **317**, 1192
Thurgood, J. O. & McLaughlin, J. A., 2012, Astron. Astrophys., **545**, A9
Thurgood, J. O. & McLaughlin, J. A., 2013, Solar Phys., accepted, DOI=10.1007/s11207-013-0298-4